JOURNAL OF MATERIALS RESEARCH AND TECHNOLOGY 2022;18:896–908

Available online at www.sciencedirect.com

jmr&t Journal of Materials Research and Technology

journal homepage: www.elsevier.com/locate/jmrt

Original Article

Effect of graphene on thermal stability of tin selenide

Manal Alsalama [a,*], Hicham Hamoudi [b], Ahmed Abdala [c], Khaled M. Youssef [d]

[a] Department of Sustainable Development, Hamad Bin Khalifa University, Doha, 5825, Qatar
[b] Qatar Environment and Energy Research Institute, Doha, 34110, Qatar
[c] Department of Chemical Engineering, Texas A&M University, Doha, 23874, Qatar
[d] Department of Materials Science and Technology, Qatar University, Doha, 2713, Qatar

ARTICLE INFO

Article history:
Received 3 October 2021
Accepted 8 February 2022
Available online 1 March 2022

Keywords:
Thermal stability
Bloating
Milling time
Tin selenide
Graphene

ABSTRACT

The thermal stability of polycrystalline tin selenide (SnSe) is essential for its long-term applications. In this study, the thermo-mechanical stability of hot compacted polycrystalline SnSe and SnSe/graphene nanocomposite is evaluated. All samples were prepared using a combination of mechanical alloying and hot compaction under an argon atmosphere. A severe bloating behavior was observed in the pristine SnSe hot compacted disks after post densification annealing. Consequently, these disks exhibited volume expansion and a drop in density, resulting in the formation of pores and cracks within the sample, which significantly degraded the electrical performance with consecutive thermal cyclings. Interestingly, the bloating behavior was reduced upon the incorporation of graphene within the SnSe matrix. However, this reduction was limited to samples with a homogeneous distribution of graphene. Dilatometer measurements showed that the as-compacted SnSe/graphene nanoplatelets (GNPs) sample in which graphene was milled for 4 h exhibited less hysteresis than the pristine SnSe sample. Accordingly, the electrical performance of the SnSe/GNP samples was more stable than the pristine SnSe after consecutive thermal cycles. The obtained results indicate that homogeneously distributed graphene plays a significant role in improving the thermal stability of the SnSe-based nanocomposite.

1. Introduction

Thermoelectric materials have attracted significant interest owing to their capability to convert heat to electricity. These materials provide an alternative sustainable energy resource by effectively collecting and utilizing waste heat as a major fuel for supplying power. Although research on thermoelectric materials has mainly focused on characterizing and enhancing their thermoelectric performance, it is equally

* Corresponding author.
E-mail addresses: manalalsalama@gmail.com, malsalama@hbku.edu.qa (M. Alsalama).

https://doi.org/10.1016/j.jmrt.2022.02.045

Table 1 – Uncertainties values in the measured properties of SnSe based material.

Sample	Uncertainty value	Reference
Zn-doped SnSe	12% in ZT	[30]
Ag-doped SnSe	20% in ZT	[36]
Ge-doped SnSe	18% in ZT	[37]
K-doped SnSe	15–20% in ZT and density	[5]

important to evaluate their reliability. Owing to the nature of their application, thermoelectric materials are continually subjected to consecutive heating and cooling cycles over a wide range of temperatures. This may result in high mechanical internal stresses, which affect their mechanical stability [1]. Therefore, in addition to high thermoelectric performance and high energy conversion efficiency, thermoelectric materials with excellent mechanical stability, low thermal degradation, and low coefficient of thermal expansion [2,3] are essential for their successful applications in power generation devices with longer lifetimes.

In addition to the direct effect of material synthesis techniques on the overall thermoelectric performance of the thermoelectric materials, it has been found that thermomechanical properties are also affected by the synthesis method. Powder processing techniques, such as milling, efficiently produce nanosized grain materials, which can significantly enhance the thermoelectric performance [4]. However, fine powders cause specific problems during their processing. The powder synthesized through mechanical milling generally has a high surface area and high chemical reactivity due to the highly refined grains; therefore, they accumulate energy and can easily absorb oxygen and other impurities [5]. Moreover, powder particles exhibit a large intra-space between the particles that could trap gases during the consolidation process [6–9]. When high pressures are applied during compaction, the entrapped gas is compressed in the pores, and the closed pores shrink until the pressure of the entrapped gas becomes equal to the applied pressure [6,10]. Upon thermal annealing in the absence of applied pressure, the pressure of the entrapped gas (whether caused by the external trapped gas from the compaction atmosphere, the decomposition of the oxide, or the material itself) increases. Further, if the pressure is sufficient to plastically deform the material, it causes swelling, which is sometimes referred to as “foaming” or “bloating.” This bloating leads to the formation of pores and cracks, a drop in density, and hysteresis in thermal expansion [6–8]. The dimensional instability associated with bloating may lead to severe stresses. Therefore, measuring the thermal expansion could help identify the bloating behavior of the thermoelectric materials [6].

Bloating behavior of thermoelectric materials has been reported in the literature. Witting et al. [11] reported a much higher density drop of 8% in pellets produced from ball-milled bismuth telluride ($Bi_{0.5}Sb_{1.5}Te_3$) when annealed at 300 °C for 24 h compared to a density drop of 1% in powders produced by hand grinding using an agate mortar and pestle. The observed density drop was attributed mainly to the volume expansion. The mechanism through which ball milling induces swelling is not clearly understood. However, one possibility could be the trapped argon gas within the powder particles during the milling process. Similar behavior has been observed in PbTe based materials in different studies [4,12]. Schmitz et al. [12] reported a substantial density reduction and volume expansion of lead telluride (PbTe) after thermal cycling, which reduced the thermal conductivity. Ni et al. [4],in another study, reported a degradation in thermoelectric properties of PbTe-based material upon annealing because of trapped oxygen on the as-milled particle surfaces during sintering. It is worth mentioning that the expansion of the trapped gas is a common process of solid-state foaming by annealing the compact, made through the hot isostatic pressing of powder in an overpressure of argon [9]. Furthermore, bloating can be produced as a result of material sublimation or decomposition during annealing. Samuel et al. [13] reported foaming of nanocrystalline bismuth telluride (Bi2Te3) upon heating as a result of phase decomposition to a certain extent to form a Te-rich equilibrium compound. The evaporation of Te generated pressure that led to the evolution of pores.

Porosity in thermoelectric materials is undesirable since it is generally deleterious to thermoelectric performance [4,9,12]. Pores typically scatter the electrons more than the phonons; hence, the porosity can significantly affect the thermoelectric performance [9,14]. Lee et al. [15] reported a significant reduction in both the electrical and thermal conductivities and an enhancement of the Seebeck coefficient with increasing porosity in silicon-germanium (SiGe) alloys. However, the Seebeck coefficient's enhancement was not sufficiently large to compensate for the reduction in electrical conductivity; hence, the overall ZT value was degraded. In addition, porous solids are less mechanically robust than fully

Table 2 – Notation of prepared samples based on graphene milling time.

Disk Sample Code	Sample description
GNP-1m	SnSe/GNP nanocomposite, graphene milled for 1 minute.
GNP-10m	SnSe/GNP nanocomposite, graphene milled for 10 minutes.
GNP-1h	SnSe/GNP nanocomposite, graphene milled for 1 hour.
GNP-2h	SnSe/GNP nanocomposite, graphene milled for 2 hours.
GNP-4h	SnSe/GNP nanocomposite, graphene milled for 4 hours.

Table 3 – Raman spectroscopy data for as-received GNPs and SnSe/GNPs composites with different milling times.

Sample	Raman Shift (cm^{-1})			Intensity Ratio	
	D	G	2D	I_D/I_G	I_{2D}/I_G
GNP-4h	1343.2	1577.5	2676.7	1.169	0.44
GNP-2h	1350	1580	2690	0.945	0.65
GNP-1h	1342.2	1572.7	2685.4	0.690	0.61
GNP-10m	1341.3	1570.8	2690.2	0.362	0.50
GNP-1m	1338.382	1568.834	2671.917	0.303	0.51
As-received GNPs	1346	1577.5	2706	0.260	0.522

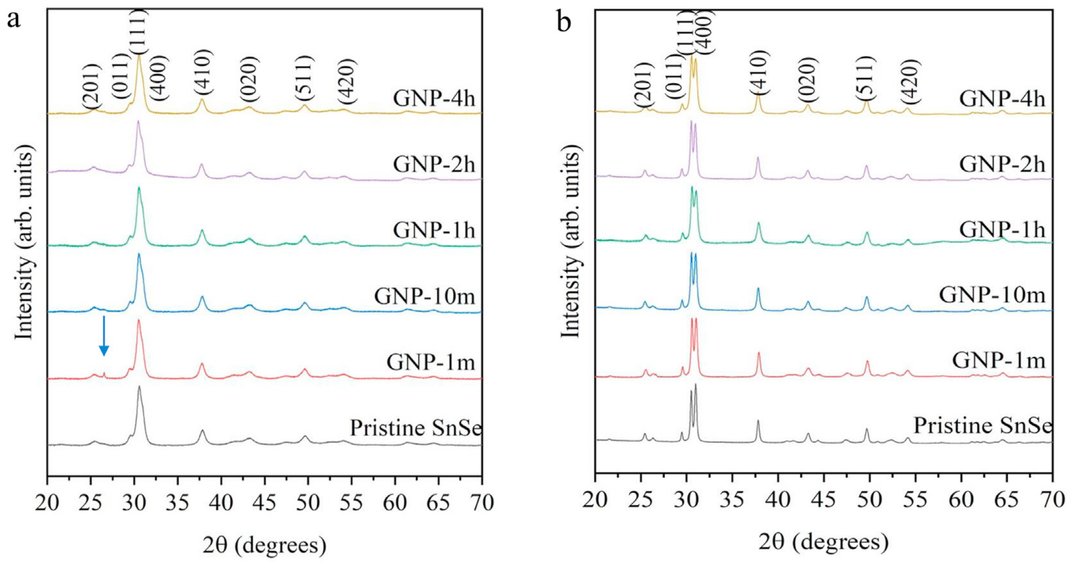

Fig. 1 – a XRD for the pristine SnSe, the as-received GNP, and the SnSe/GNPs composites at different graphene milling times. The marked (002) plane peak in the GNP-1m sample is well matched with (002) plane peak of GNP, b) XRD for the compacted pristine SnSe, and the SnSe/GNPs composites at different graphene milling times.

dense solids, which leads to the formation of cracks and eventually to device failure [9].

Graphene—a two-dimensional (2D) material—has been widely used as a nanofiller in thermoelectric systems for the enhancement of thermoelectric properties. Beyond of its role on enhancing thermoelectric properties, graphene can also contribute to the thermal stability of thermoelectric composites. Jagadish et al. reported that incorporating 0.1 wt% of

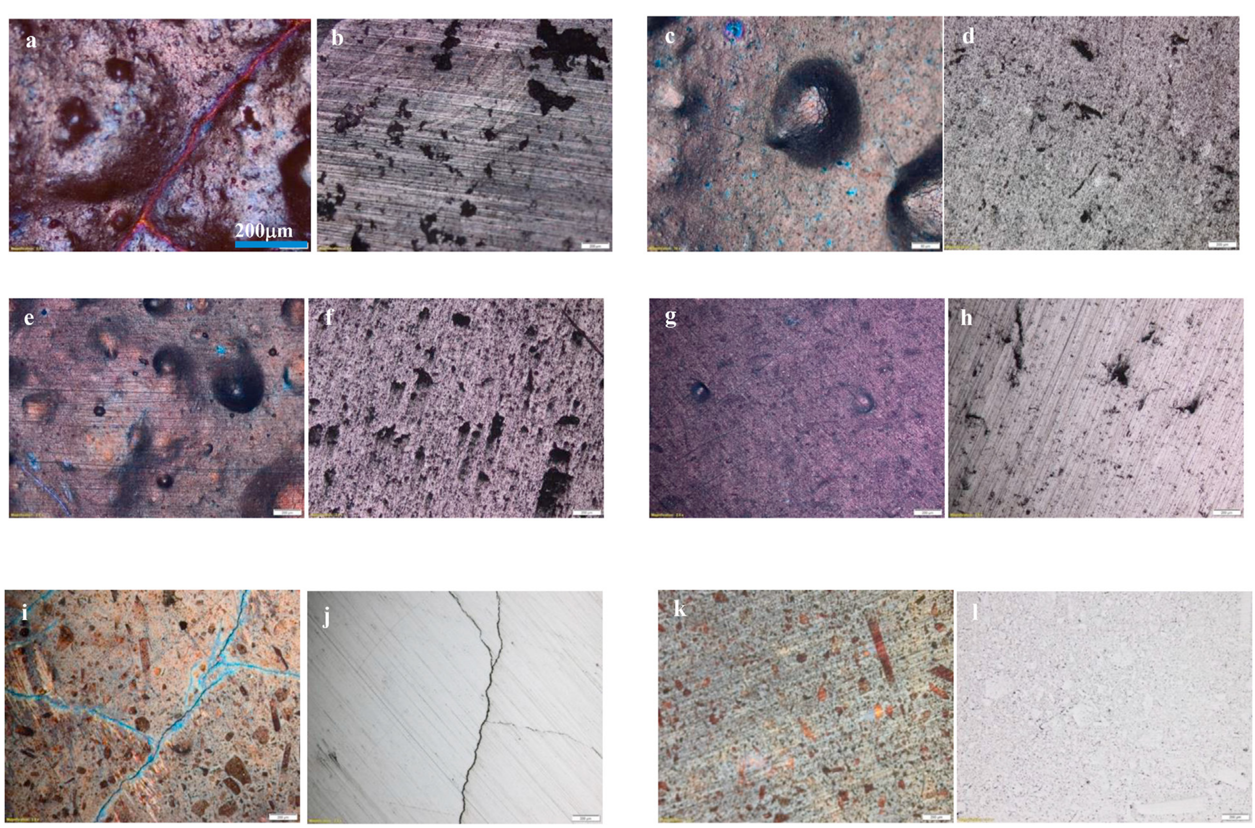

Fig. 2 – Optical microscopic images before and after polishing, of thermally cycled a,b) pristine SnSe, c,d) GNP-1m, e,f) GNP-10m, g,h) GNP-1, i,j) GNP-2h, and, k,l) GNP-4h, showing bubbles, cracks and pore morphology. Scale bar is 200 μm in all images.

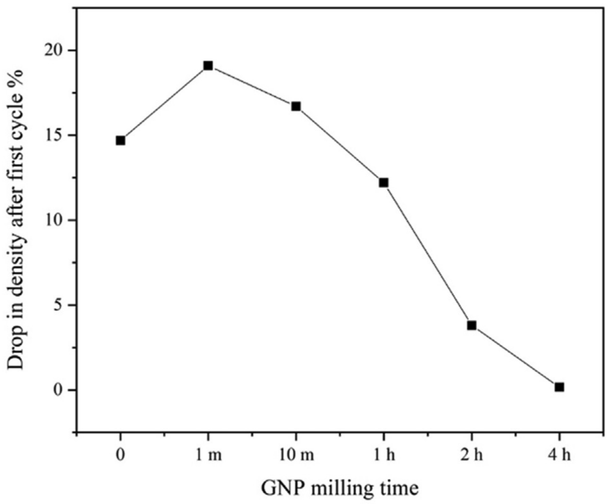

Fig. 3 – Percentage drop in density for SnSe-1, GNP-1m, GNP-10m, GNP-1h, GNP-2h, and GNP-4h.

graphene in a bismuth sulfide (Bi_2S_3) matrix enhanced the thermal stability of the material and shifted all the Derivative Thermogravimetry (DTG) curves to the right [2]. Polymer graphene composites can sustain a wide range of temperatures. The incorporation of graphene in epoxy resins resulted in a low coefficient of thermal expansion while maintaining the high thermal stability of the material [16]. However, to achieve the best functionality of graphene, it should be distributed homogeneously and achieve good interfacial bonding with the matrix. Agglomeration of graphene owing to its high specific area and flexible 2D nature limits its functionality. Among several techniques that have been used to incorporate graphene in the matrix of a composite, ball milling, owing to its simplicity, flexibility, scalability, and cost-effectiveness, has been widely used for the successful preparation of several composites with well-dispersed graphene [17,18]. Milling produces shear forces and causes collisions that help exfoliate graphene sheets and prevent graphene sheets agglomeration. It has been found that well-dispersed graphene can significantly enhance the thermoelectric performance of a composite. Tang et al. [19] reported excellent cyclic performance and enhanced thermal stability of copper sulfide (Cu2S) when incorporated with a homogeneous distribution of graphene.

Tin selenide (SnSe) is a promising thermoelectric material that has attracted significant attention due to its abundance and composition of non-toxic elements with a high thermoelectric figure of merit (ZT) reported for its single crystal form [20]. Nonetheless, a single crystal of SnSe is not suitable for thermoelectric devices, owing to the special conditions of the single crystal growth technique. such as expensive production, poor cleavage, and high anisotropy along different crystallographic directions. All these issues have initiated much interest in producing polycrystalline SnSe with better mechanical properties and easily controllable production for practical applications by creating nanostructured SnSe [21–23] and doped SnSe [24–31], as well as nano-composites [32–34]. However, the reliability of polycrystalline SnSe and its compoites upon multi thermal cycles has not been evaluated in literature. Several studies have reported some

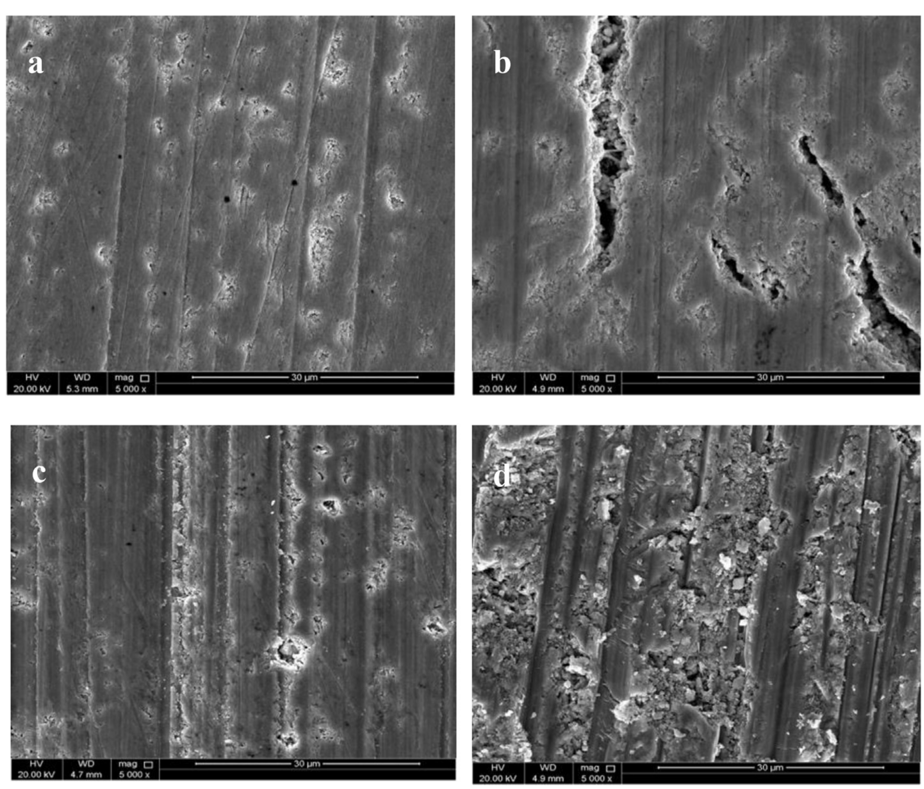

Fig. 4 – Cross-sectional SEM images of a) as-compacted SnSe, b) SnSe after first thermal cycle, c) as-compacted GNP-4h and d) GNP-4h after first thermal cycle.

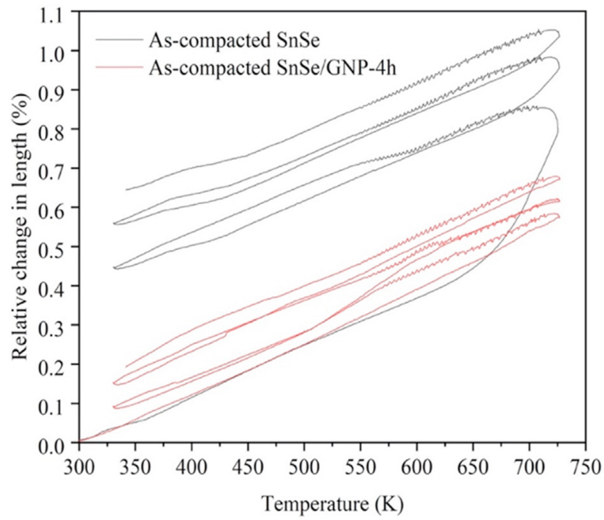

Fig. 5 – Relative dimensional change for consecutive two heating and cooling cycle a as a function of temperature for as-compacted SnSe and GNP-4h samples.

uncertainty in the thermoelectric properties and density measurements of SnSe. In one study, Cai et al. [35] reported a 5% uncertainty in Seebeck coefficient, electrical conductivity, and density measurements owing to the volume expansion of SnSe. Other studies reported different values of uncertainties, summarized in Table 1, but no data about the density or dimensional expansion have been reported. Although part of the uncertainty can be attributed to errors in the measurement, the effect of bloating cannot be excluded, and it may cause part of the error in the measurement.

Despite many reports of thermally induced porosity and volume expansion in thermoelectric systems, to the best of our knowledge, no systematic studies of the bloating process have been reported. Furthermore, there is a lack of studies on the thermal stability of hot compacted polycrystalline SnSe and SnSe/graphene nanoplatelets (GNPs) nanocomposite. In this study, we report the effect of graphene nanoplatelets on the thermal stability and the thermoelectric performance of SnSe prepared by mechanical milling and hot compaction techniques. Further, we investigate the effect of GNPs and their processing time on the thermal stability of the SnSe/GNPs nanocomposite after two consecutive thermal cycles. The crystal structure, elemental composition, and electrical transport properties of various annealed samples are characterized, and their thermal stabilities are evaluated.

1.1. *Experimental work*

Nanobulk polycrystalline SnSe and polycrystalline SnSe/GNPs nanocomposite (SnSe/0.5 wt% GNPs) powders were fabricated through mechanical milling of the elemental powders of Sn (99.995%, Nanoshel), Se (99.999%, Alfa Aesar), and GNPs, and all powders were purchased from Sigma–Aldrich. The powders were weighed in a glove box under a high purity argon atmosphere ($O_2 < 0.5$ ppm) and loaded into stainless vials with a ball-to-powder ratio of 10:1. The pristine SnSe powder and SnSe/GNPs composite were milled for 12 h. To prepare the SnSe/GNP nanocomposite, different samples were mechanically milled with graphene for different durations (1 min, 10 min, 1 h, 2 h, and 4 h). The consolidation of the samples was performed using hot pressing. The milled powders were loaded into a tungsten carbide die with a diameter of 12.7 mm and thickness of 3 mm and were compacted under a uniaxial pressure of 1 GPa and at a temperature of 773 K for 10 min. The prepared samples and the milling conditions are listed in Table 2.

The crystal structure and phase identification of the milled samples were investigated using X-Ray Diffraction (XRD) (PANalytical, EMPYREAN) at 298 K within the 2θ range of 20°–70° (see Table 3). The degree of crystallinity and structural defects in graphene were examined by Raman spectroscopy (RS: Thermo Fisher, DXR) at a wavelength of 532 nm and a laser power of 10 mW. The morphology and structural characteristics were investigated through scanning electron microscopy (SEM) (Nano-SEM Nova 450, FEI-USA). The evolution of the pore structure was investigated using an optical

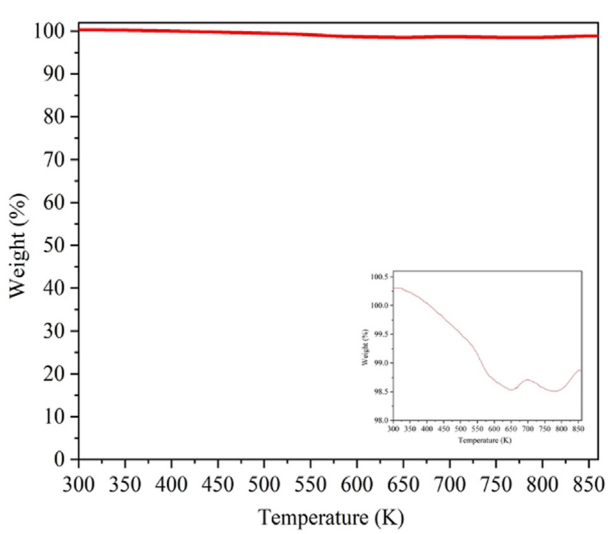

Fig. 6 – TGA curve for pristine SnSe, inset is curve magnification between 98% and 100% weight.

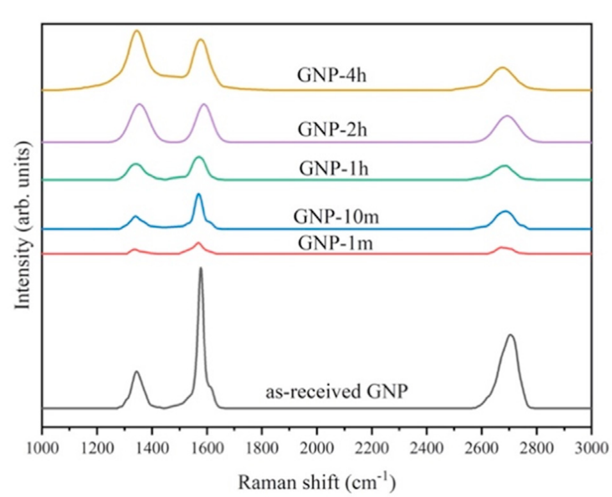

Fig. 7 – Raman spectra of as-received graphene and as-milled SnSe/GNPs composites at different milling times.

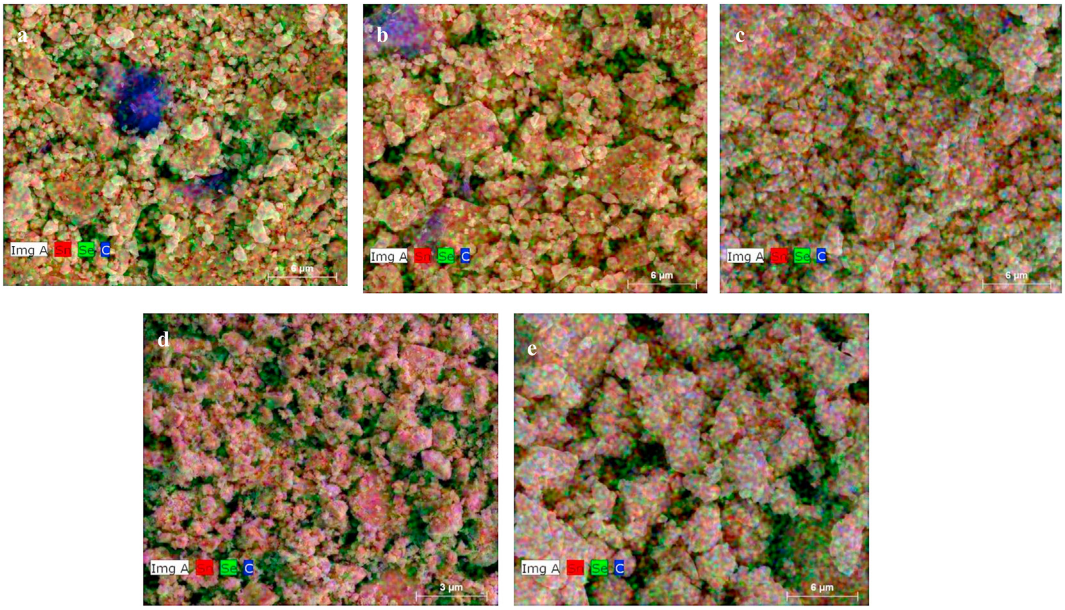

Fig. 8 – SEM-EDS elemental mapping analysis images of the as-milled powder of a) GNP-1m, b) GNP-10m, c) GNP-1h, d) GNP-2h, and e) GNP-4 h.

microscope (OLYMPUS, BX53M). An FEI-TECANI G2 FEG and a field emission gun TALOS (FEI, Hillsboro, Oregon, USA) equipped with a high-angle annular dark-field (HAADF) detector and an FEI energy dispersive X-ray (EDX) detector transmission electron microscope (TEM) were used to investigate the microstructure and the elemental distribution in the processed samples. Both devices were operated at 200 kV. An Esprit software from Bruker (Billerica, Massachusetts, USA) was used to perform the quantitative elemental analyses. The TEM samples were prepared by dispersing a small amount of the powder sample in isopropyl alcohol and sonicating it using an Ultrasonication bath for 10–20 min. Then, 10 uL of the dispersed solution was drop-casted on a carbon film copper grid of 300 mesh using a micropipette.

Thermogravimetric analysis (TGA) of the powder sample was performed in the temperature range of 298 K–873 K at a heating rate of 20° Celcius per minute under a nitrogen atmosphere. The thermal expansion was evaluated using a dilatometer (DIL 106 from TA instruments) at temperatures ranging from 298 K to 773 K. The sample density was calculated by the Archimedes method using a Sartorius density determination kit (Sartorius YDK03, Germany). The density determination kit was set up using distilled water, and the water temperature was monitored during the measurement. For power factor measurements, the Seebeck coefficient and the electrical conductivity of the consolidated samples were measured simultaneously using SBA 485 Nemesis–NETZSCH. These measurements were performed at room temperature–773 K under an ultra-high purity argon atmosphere.

2. Results and discussion

The XRD patterns of the as-milled pristine SnSe, and SnSe/GNP nanocomposites in which graphene was added at different stages of milling are shown in Fig. 1a. The XRD peaks of all the samples show fundamental peaks that are typical to the orthorhombic SnSe phase with space group Pmna (JCPDS card number 48–1224). No extra peaks belong to a second phase or contamination from the milling process were detected. However, the signature (002) graphene peak was only observed in the XRD pattern of the SnSe composite where graphene was added at the last 1 min (peak is marked in Fig. 1a). The presence of the graphene peak in this sample may be attributed to the agglomeration of graphene in this sample which agrees with the results obtained for milled $Bi_{85}Sb_{15}$-0.08%Gr composite [38]. The absence of graphene (002) peak in composite samples could be attributed to the low concentration of the distributed graphene that could not be detected by XRD [39] or to the loss of graphene crystallinity with milling time [40]. The broadening of the peaks indicates the refinement of the grain size. This was analyzed by estimating the grain size using XRD data and the Warren- Averbach method [41]. The calculated average grain size values were 10 ± 2 nm for the pristine SnSe and SnSe/GNP composites indicating the effectiveness of milling for producing very fine nano bulk materials. The prepared powder samples were consolidated using hot pressing as explained in the experimental section. To ensure the structural stability of the prepared samples after the hot compaction, the crystal structure and phases analysis of the compacted disks were investigated by XRD, and the obtained patterns are presented in Fig. 1b. Compared to the as-milled samples, the XRD peaks of the compacted disks become narrower, which implies a possible grain growth. The calculated average grain size was 29 ± 2 nm, which is higher than the as-milled grain size value but still in the nanoscale range. However, all peaks are related to the same reference of the pristine sample; thus, no contamination or phase changes from the compaction process occurred. Thermal behavior of the hot compacted disks of pristine SnSe, GNP-1m, GNP-10m, GNP-1h, GNP-2h, and GNP-4h was studied by thermally cycled the disks from room temperature to 773 K. After heating, all the disks exhibit significant changes in their surface structures such as the presence of bubbles and cracks. Figure 2 shows the optical microscopic images of the SnSe, GNP-1m, GNP-10m, GNP-1h, GNP-2h, and GNP-4h nanocomposite surfaces after one heating cycle before and after polishing. Bloating behavior was clearly observed by the

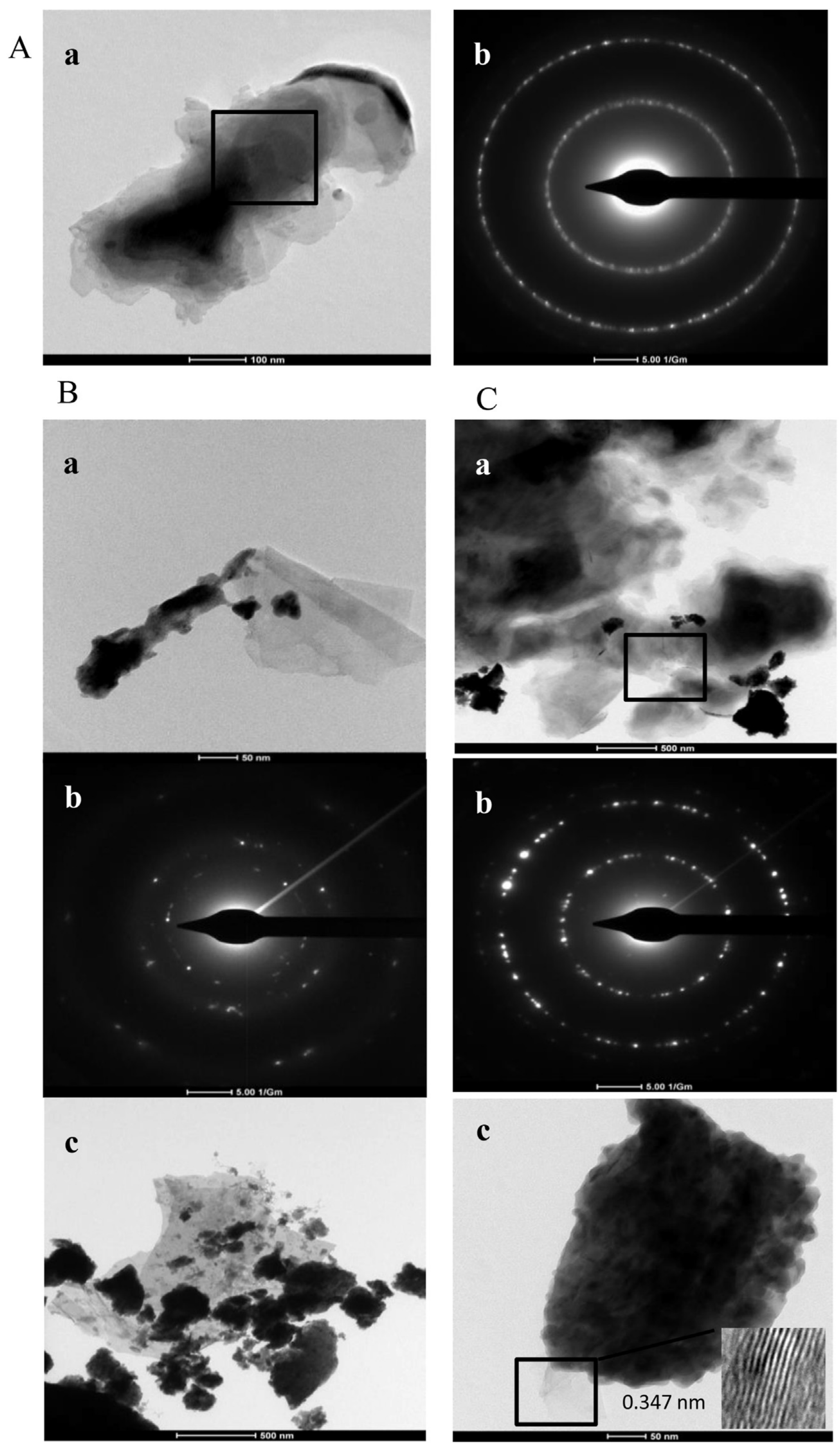

Fig. 9 – A) TEM image of the GNP-1m sample a) Bright-field image, b) the corresponding SAED pattern of the selected area from (a). GNP sheets appear to be agglomerated. B) TEM image of the GNP-10m sample a) Bright-field image, b) the corresponding SAED pattern of the selected area from (a), c) Second selected area of GNP-10m where several GNP sheets appear to be stacked. C) TEM image of the GNP-1h sample a) Bright-field, b) the corresponding SAED of (a), c) Second selected area of GNP-1h where GNP sheet (enlarged in the onset) appears to be exfoliated to very thin and transparent sheets in the circled area with interplanar distance of 0.347 nm.

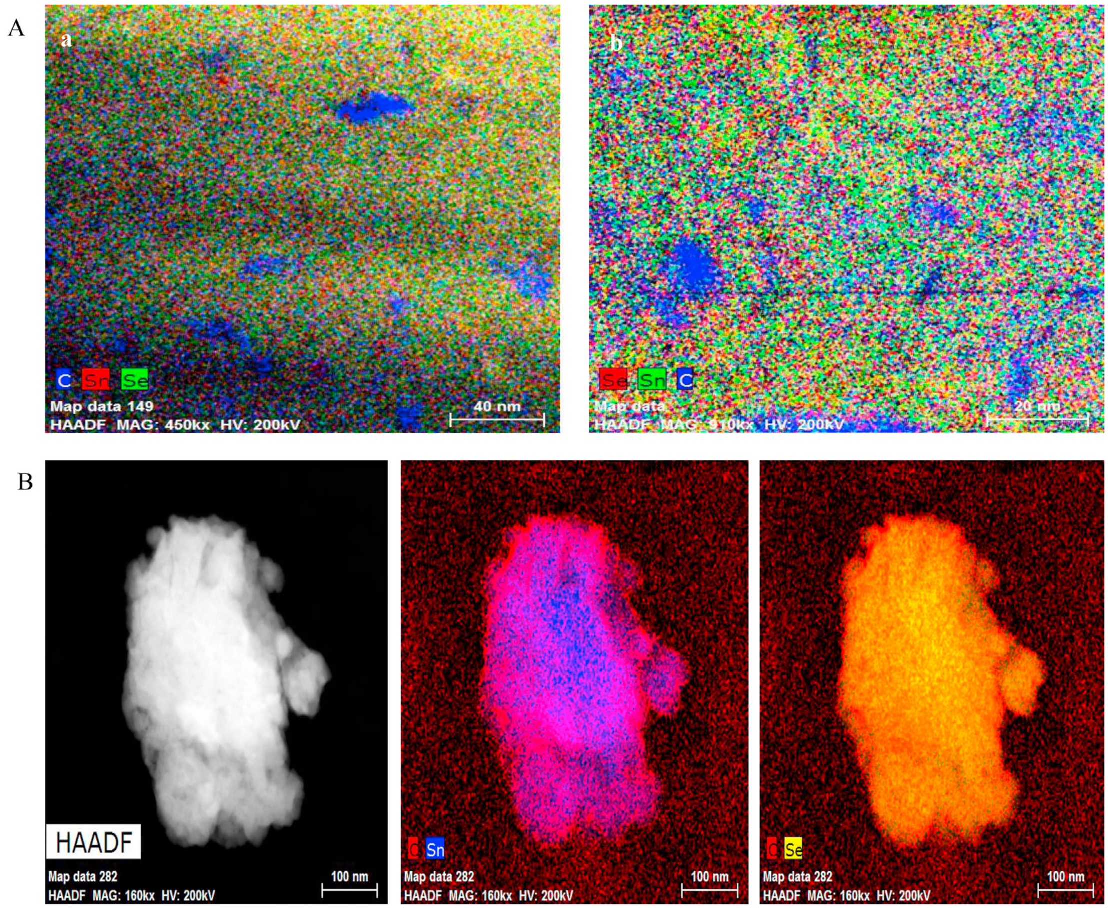

Fig. 10 – A) HAADF-STEM elemental mapping images of a) GNP-2h, b) GNP-4h showing the elemental distribution of Sn, Se, and graphene, where graphene is homogeneously distributed with a certain aggregation along the grain boundaries. B) HAADF-STEM elemental mapping image of GNP-4h showing the elemental distribution of Sn, Se, and graphene, where graphene densely exists along the particle's boundaries.

presence of bubbles and cracks on the surface of the SnSe, GNP-1m, and GNP-10 m samples, whereas pores appear on the surface of the samples after the surfaces were polished. However, bloating decreased gradually with increasing graphene milling time, for GNP-1h and GNP-2h and is almost absent in GNP-4h, as seen in Fig. 2 e, d, and f, respectively. Pores density of samples in Fig. 2 are 20%, 29%, 22%, 16%, 6%, and 0.6% for SnSe, GNP-1m, GNP-10m, GNP-1h, GNP-2h, GNP-4h, respectively. The formation of the pores may be related to the induced pressure of entrapped gas within the sample. During annealing, the gas expands and form bubbles. When the stress from the expanded gas is too high for the surface of the sample to withstand, the bubbles crack [42]. A variation in density is expected with the evolution of the pores; therefore, the density variation was calculated, and the drop in density percentage is reported in Fig. 3. Pristine SnSe exhibits an approximately 15% drop in density. The drop in density initially increases upon the addition of graphene at 1 min of milling, and then it decreases with increasing milling time until it reaches 0.16% in the GNP-4h sample.

To further elucidate the pore structure, SEM images of a small section after cutting through the cross-section of pristine SnSe and GNP-4h sample disks were obtained at high magnification. Figure 4 compares the cross-section of pristine SnSe Figure 4 (a,b) and GNP-4h Figure 4 (c,d) before and after the first thermal cycle, respectively. It is obvious that before the thermal cycle, both samples showed a well-compacted disk with no observable pores. However, after thermal cycling, the SnSe sample exhibited bloating behavior (See Figure 4b) with no significant pores in the GNP-4h sample (See Figure 4d).

In addition to the optical microscopy and SEM observations, thermal expansion measurement is a helpful method for identifying bloating behavior. Bloating in this study was measured directly using a dilatometer by thermally cycling both the SnSe and SnSe-4h samples twice from room temperature to 773 K. The data are presented in Fig. 5. The dilatometric measurements reveal significant hysteresis between heating and cooling for the SnSe sample as a progressive increase in the specimen length at the end of each thermal cycle, which is consistent with the bloating behavior. Similar hysteresis behavior as a result of bloating and gas expansion has been reported for hot-pressed lead telluride-based materials (PbTe–PbS) [6] and $Co_{0.95}Pd_{0.05}Te_{0.05}Sb_3$ [10]. Since the SnSe sample is single-phased, there is no possibility that thermal expansion mismatch is responsible for this bloating and cracking behavior. The only possibility for the observed increase in length is post-densification bloating, which is

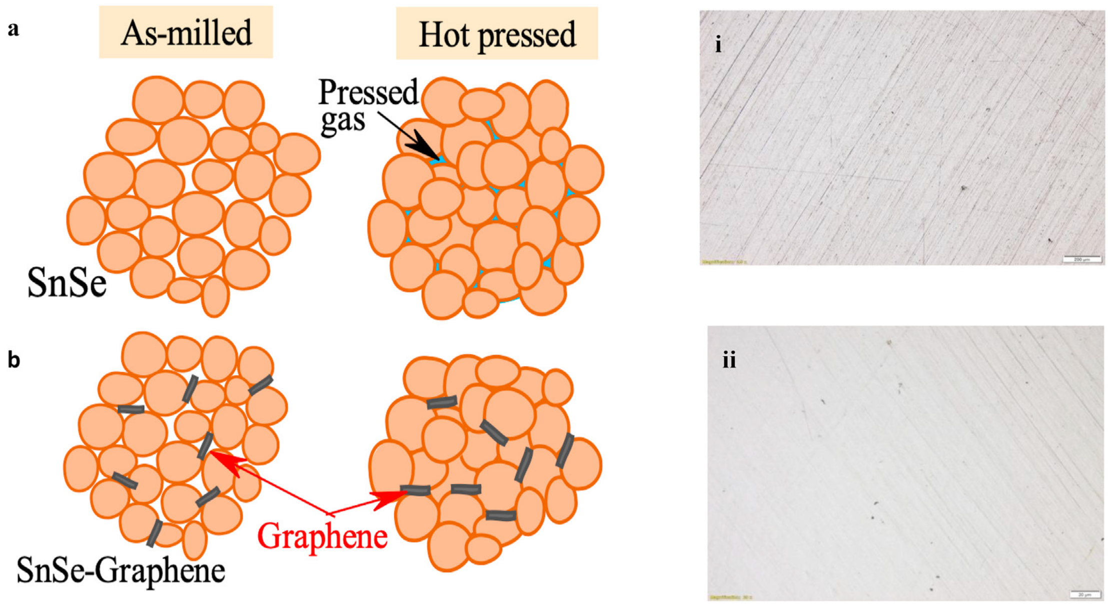

Fig. 11 – Schematic illustrations of consolidation mechanism of a) SnSe sample with corresponding as-compacted surface optical image (i), b) GNP-4h with its corresponding as-compacted surface optical image (ii).

consistent with the porosity observation by SEM. However, the hysteresis in GNP-4h is significantly smaller due to the incorporation of graphene within the matrix.

To investigate whether the bloating is a result of the expansion of entrapped gas or material loss, TGA was conducted on pristine SnSe. The plot of weight loss versus temperature from TGA is shown in Fig. 6. It can be seen that the mass decay is very small during the heating process. Weight loss of approximately 1.5% at 653 K followed by a weight gain of approximately 0.25% at 693 K is observed. The weight change is caused by a combination of two factors: weight gain that occurs by picking up oxygen from the air to form oxides and weight loss due to the sublimation of Sn-containing oxides [43]. The considerably small weight change indicates that the bloating behavior corresponds to the expansion of the gas, and not to the mass loss of either SnSe or any impurities or oxides that could sublimate during annealing.

To investiagate the effect of milling time on enhancing the bloating behavior, the integrity and distribution of graphene were analyzed by Raman spectroscopy, SEM, and TEM for the SnSe-1m, SnSe-10m, SnSe-1h, SnSe-2h, and SnSe-4h composites. Figure 7 shows the Raman spectra of graphene for all composite samples compared to that of the as-received GNP. The Raman spectra show three characteristic peaks of graphene around 1350, 1570, and 2700 cm-1, which correspond to the disordered band (D), the graphitic band (G), and another graphene characteristic band (2D), respectively. However, the intensities of the peaks vary with the milling time. The 2D and G peaks are weakened and broadened, and the D band gradually becomes the most prominent peak in the Raman spectra. This indicates the increasing amount of the introduced defects and disorders into graphene structure with milling time [44–46]. Table 2 summarizes the intensity ratio of ID/IG and I_2D/IG that provides an estimation of the structural integrity of graphene and the thickness of the graphene sheets, respectively. From the calculated data, the lowest ID/IG (0.26) is for the as-received GNPs, followed by a slightly higher value of 0.303 for the GNP-1m sample. This suggests that graphene preserves its crystallinity in this sample. The ID/IG increases gradually with increasing milling time until it reaches 1.169 for GNP-4h. This indicates that milling has a significant effect in inducing a high degree of defects and disorders in the graphene structure. Moreover, the intensity ratio of the I_2D/IG in the as-received GNPs is 0.552, thereby implying that the as-received graphene is multilayered. The ratio decreases to 0.51 and 0.50 for GNP-1m and GNP-10m, respectively, thereby suggesting agglomeration and a multilayer structure of graphene [47]. However, the ratio increases to 0.61 and 0.65 with longer milling times (1 and 2 h, respectively), suggesting that graphene was exfoliated to a few layers [17,48]. Upon increasing the milling time to 4 h, the I_2D/IG decreases to 0.44, which may indicate extra folding and bending of graphene sheets with milling [49,50]. These findings are in agreement with the previously reported Raman analyses for the effect of milling on the graphene structure [18,48,51] and are expected due to the nature of the milling technique that induces intensive mechanical forces and leads to fracturing and deformation of the graphene [52].

SEM-EDS analysis was performed to further study the morphology and distribution of graphene in the composite samples. The SEM-EDS images of SnSe-1m, SnSe-10m, SnSe-1h, SnSe-2h, and SnSe-4h nanocomposites are shown in Fig. 8 (a, b, c, d and e), respectively. The SEM-EDS images indicate that for short milling times (i.e., 1 min and 10 min) graphene appears as agglomerated sheets and clusters within the matrix. This indicates that for short milling times, graphene was able to preserve its structure; however, it was not distributed evenly within the sample. Upon increasing the milling time to 1 h and more, no graphene sheets are

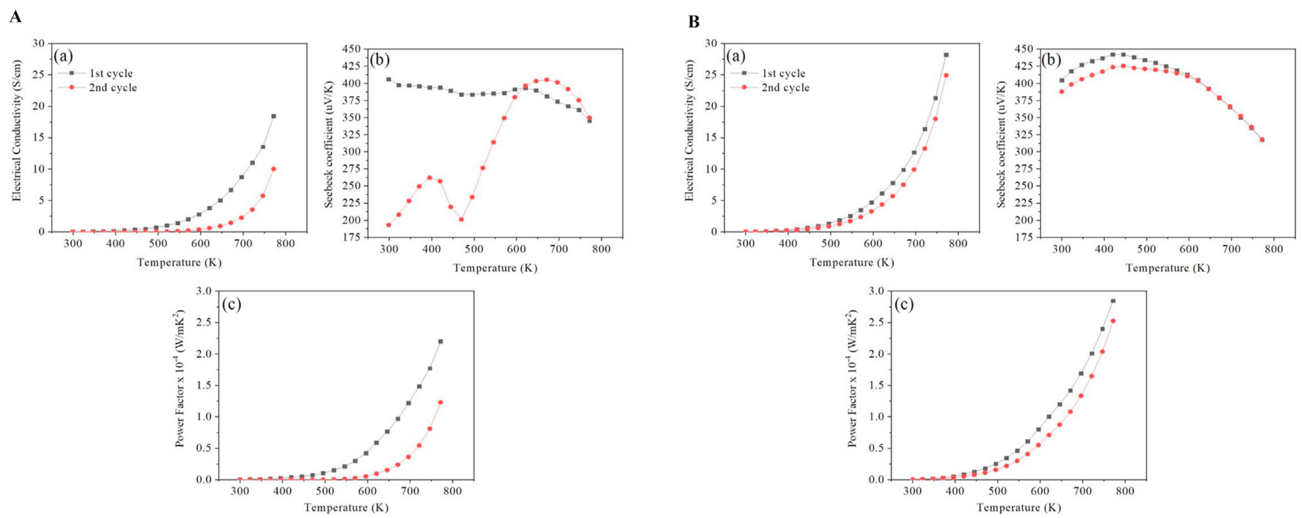

Fig. 12 – Temperature dependency of a) electrical conductivity, b) Seebeck coefficient, and c) power factor for A) pristine SnSe, and B) GNP-4h with two consecutive thermal cycles.

observed. Instead, graphene appears to be fragmentized and distributed homogeneously within the matrix. The absence of the sheets could be attributed to the severe fragmentation and plastic deformation caused by the extensive milling time. These images are in good agreement with the Raman spectroscopy results that confirm the fracturing and disordering of graphene structure with milling.

The SnSe/GNP composite nanoparticles were further characterized by TEM to investigate the graphene integrity and structural evolution with respect to the milling time. Dark-field images for GNP-1m, GNP-10m, and GNP-1h, along with selected area diffraction patterns, were obtained for the area where graphene was present. Figure 9A (a) shows the bright-field (BF) TEM image of GNP-1m, in which graphene appears to be agglomerated and wrapping the particles of SnSe, which agrees well with the XRD data. The presence of graphene sheets indicates that graphene was able to maintain its integrity, whereas its agglomeration implies that 1 min is not enough to exfoliate the graphene sheets and distribute them homogeneously. The corresponding selected area diffraction pattern (SAED) (Fig. 9A (b)) exhibits multiple individual spots, which are attributed to multilayer randomly stacked graphene. Figure 9B (a) shows the BF-TEM images of the GNP-10m sample, in which graphene appears to form multi-sheets in some areas and exfoliated sheets in other areas. The presence of these spots in the corresponding diffraction pattern indicates the preserved crystallinity of graphene with 10 min of milling. The observed agglomeration of graphene led to poor adhesion between graphene and the matrix and formed many pores that may trap extra compressed gas [53]. This is a good explanation for the higher density drop in the GNP-1m and GNP-10m samples compared to the pristine sample. Figure 9C (a) shows the BF-TEM images of the GNP-1h sample. Graphene appears to be stacked and folded to several layers of graphene in one area (Fig. 9C (a)), whereas in another area of the sample, graphene is exfoliated to a very thin transparent sheet attached to the particle (Fig. 9C (c)) with a 0.347 nm interplanar distance corresponding to (002) plane of graphene. The exfoliation of graphene with less agglomeration results in better distribution of graphene and excellent interfacial bonding with the composite matrix. The corresponding SAED pattern of multilayer graphene exhibits several spots that form a semi-full ring pattern. This pattern is mainly attributed to the several defects present in polycrystalline materials [54,55] that contain several grains in different orientations [56]. The presence of dislocation is expected during milling and agrees with the Raman spectroscopy results that showed an increase in the ID/IG ratio with respect to milling time [54,57]. Upon increasing the milling time to 2 and 4 h, no graphene sheet structure is detected in the TEM images, which indicates that the integrity of graphene has been destroyed with milling. This is in agreement with the ID/IG ratio calculated in this study from Raman spectroscopy that shows the increasing of defects and disorders in graphene and is also in agreement with the images of SEM analysis for GNP-2h and GNP-4h samples that shows the homogenous distribution of graphene within the matrix. However, the small graphene fragments have been detected by elemental mapping analysis for ion thinned particles of both the GNP-2h and GNP-4h samples, as shown in Fig. 10A (a) and (b). These images present small fragments of graphene that are homogeneously distributed within the matrix with significant aggregation at the grain boundaries. Further detection of graphene has been performed on a large scale in GNP-4h using EDAX elemental color mapping during scanning transmission electron microscopy (STEM) imaging. Figure 10B shows the presence of graphene concentrated along the particle boundaries, which could facilitate the densification process by enhancing the contact area between the particles. Since the milling time of graphene is the only variable among the analyzed samples, the enhanced thermal stability and lower pore formation with increasing milling time can be attributed to the enhanced distribution of graphene within the samples. This assumption has been confirmed by the previous structural analysis and can be explained in the following section with the help of the schematic illustration in Fig. 11. Figure 11 illustrates the consolidation mechanism of pristine SnSe and GNP-4h composite. If we assume that the composite particles are spherical, there are several voids between the particles that can capture the gas particles. With the application of high pressure, the gas particles are compressed between the composite particles until the area is completely compacted. This is illustrated in the optical microscopic image of the surface of as-compacted pristine SnSe in Fig. 11 i. It can be seen that the surface appears highly dense, and its measured density is 99.1% of the calculated theoretical density. It is well known that the entrapped gas prevents complete densification [9]. Thus full density was not achieved due to the competition of the internal gas pressure and sintering stress. Although the compacted disk exhibits high density, post pressureless annealing results in expansion of the compacted gas and a consequence drop in density. On the other side, GNP-4h sample exhibits high density with 99.4% of the calculated theoretical density, as appears in Fig. 11 ii. However, the well-dispersed graphene located along the particles' boundaries improved the desification process, filling the intrapartilcle voids, thus reducing the amount of entrapped gas. Thereby, upon annealing, very less amount of entrapped gas is expanded resulting in a very small value of density drop. Further explanation can be given based on the flexible nature of the graphene sheets. Owing to its flexibility, graphene sheets can be easily incorporated in non-uniform shape voids, thereby preventing the gas from penetrating the voids. In addition, several previous studies reported that carbonic materials like carbon nanotube and graphene has a lubricant effect. This lubricant effect facilitates the densification of the composites when any of the carbonic material is incorporated within a matrix [58], but the exact mechanism of densification is not well investigated and understood. For example, Sun, Jialin, et al. reported an enhancement of densification for Titanium carbide and Tungsten carbide upon the incorporation of graphene. The lubricant characteristic of graphene plays a role in enhancing the arrangement of the particles [59]. Similarly, Yadhukulakrishnan et al. [60] reported the enhancement in the densification of GNPs reinforced zirconium diboride composite as a result of the self-lubricant effect of graphene. Dong et al. reported an improvement of copper-tungsten densification with the additive of graphene. The improvement was attributed to the rearrangement of the tungsten particles due to their good wettability with graphene. However, in the case of short milling time graphene composite, agglomeration of graphene at a specific area in the sample may trap extra gases between the graphene layers and within the folded area, as observed in the case of the GNP-1m. Any agglomeration of graphene may lead to weakening contact area between matrix particles, thus increases the porosity.

To study the effect of microstructural stability on the electrical performance, the electrical conductivity and the Seebeck coefficient of the pristine SnSe and SnSe-GNP nanocomposites were measured between 300–773 K. Furthermore, the power factors were calculated for two consecutive thermal cycles for the pristine SnSe and GNP-4h samples because GNP-4h exhibits the best mechanical stability compared to other samples. The data are presented in Fig. 12. The results show a drop in the power factor (PF) for both samples in the second cycle compared to the first cycle (See Figure 12A (c) and Figure 12B (c). However, both the electrical conductivity and Seebeck coefficient show a similar trend in the second cycle compared to the first cycle for both pristine SnSe and GNP-4 h samples (See Figure 12A (a and b) and Figure 12B (a and B). The calculated percentage drop in the power factor is shown in Fig. 13. A significant drop in the power factor of the pristine SnSe sample that ranges between 99.7% at room temperature and the minimum of 44% at 773 is observed, which is in good agreement with the evolution of the pores. However, the drop in the PF for the GNP-4h sample is significantly lower, with a maximum of 38% and a minimum of 11% in the high-temperature range. This indicates that the electrical performance is stable within the measured temperature range for samples comprising graphene with long milling times. The electrical properties are directly related to the evolution of insulating pore phases. The presence of the pores plays a significant role in scattering the charge carriers and blocking their movement [62]. As a result, the drop in power factor is believed to be due to the pore evolution.

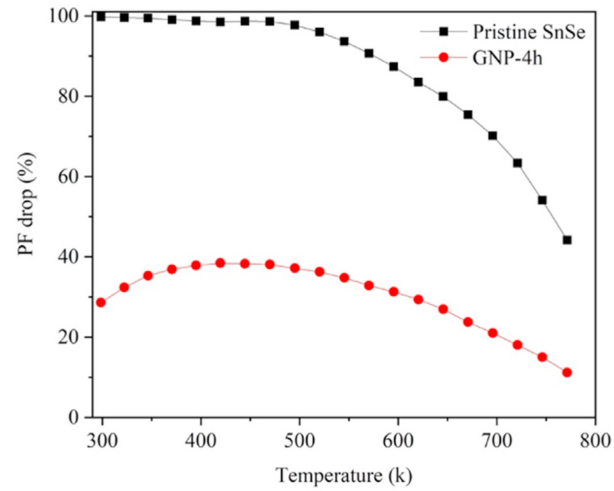

Fig. 13 – Percentage drop in PF as a function of temperature for pristine SnSe and GNP-4h.

3. Conclusion

The thermal stability of SnSe and SnSe/GNP nanocomposites prepared by mechanical milling and hot compaction was investigated in the range of room temperature to 773 K. The hot compacted disks exhibited bloating behavior upon annealing as a result of entrapped gas expansion. As a consequence, the density dropped, and the electrical performance and calculated power factor degraded with two consecutive thermal cycles. Upon the incorporation of graphene, the bloating behavior of the composite was effectively altered, and the drop in the density decreased with the increased milling time of the incorporated graphene. Consequently, the drop in the power factor was reduced, and the thermomechanical stability was enhanced. These results are attributed to the homogeneous distribution of graphene within the composite, where graphene plays a significant role in enhancing the consolidation process, filling the particles' intra-pores, thus preventing the gas from being entrapped inside the pore.

Declaration of Competing Interest

The authors declare that they have no known competing financial interests or personal relationships that could have appeared to influence the work reported in this paper.

Acknowledgment

This work was made possible by the NPRP award [NPRP10-0206-170366] from the Qatar National Research Fund (a member of the Qatar Foundation). The statements made herein are solely the responsibility of the authors. The authors would like to acknowledge the support by the Qatar Research Leadership Program (Grant no. QRLP9-G-3330017) and the technical support provided by the Central Laboratory Unit and the Center of Advanced Materials at Qatar University and the technical assistance provided by Mr. Janarthanan Ponraj and Dr. Ayman Samara at the Imaging and Characterization Core Lab, Hamad Bin Khalifa University.

REFERENCES

[1] Skomedal Gunstein, Kristiansen Nils, Engvoll Marianne, Middleton Hugh, et al. Methods for enhancing the thermal durability of high-temperature thermoelectric materials. J Electron Mater 2014;43(6):1946–51.
[2] Jagadish Jagadish, Khalid Mohammad, Phei Li Lau, Amin Nowshad, Walvekar Rashmi, Chan Andy, et al. Effect of graphene doping on the charge carrier and thermoelectric properties of RCF-Bi2S3 composites. In: AIP conference proceedings. AIP Publishing LLC; 2019.
[3] Tang Yu, Decong Li, Zhong Chen, Shuping Deng, Luqi Sun, Wenting Liu, et al. Excellent thermal stability and thermoelectric properties of Pnma-phase SnSe in middle temperature aerobic environment. Chin Phys B 2018;27(11):118105.
[4] Ni JE, Case Eldon, Stewart Rayan, Wu Chun-I, Timothy Hogan, Mercouri Kanatzidis, et al. Bloating in (Pb 0.95 Sn 0.05 Te) 0.92 (PbS) 0.08-0.055% PbI 2 thermoelectric specimens as a result of processing conditions. J Electron Mater 2012;41(6):1153–8.
[5] Chen Yue-Xing, Ge Zhen-Hua, Yin Meijie, Feng Dan, Huang Xue-Qin, Zhao Wenyu, et al. Understanding of the extremely low thermal conductivity in high-performance polycrystalline SnSe through potassium doping. Adv Funct Mater 2016;26(37):6836–45.
[6] Ni Jennifer, Case Eldon, Schmidt Robert, Wu Chun, Hogan Timothy, Trijo Rosa, et al. The thermal expansion coefficient as a key design parameter for thermoelectric materials and its relationship to processing-dependent bloating. J Mater Sci 2013;48(18):6233–44.
[7] Witting Iyan, Grovogui Jann, Dravid Vinayak, Snyder Jeffery, et al. Thermoelectric transport enhancement of Te-rich bismuth antimony telluride (Bi0. 5Sb1. 5Te3+ x) through controlled porosity. Journal of Materiomics 2020;6(3):532–44.
[8] Meshalkin VP, Belyakov AV. Methods used for the compaction and molding of ceramic matrix composites reinforced with carbon nanotubes. Processes 2020;8(8):1004.
[9] Humphry-Baker SA, Schuh CA. Spontaneous solid-state foaming of nanocrystalline thermoelectric compounds at elevated temperatures. Nano Energy 2017;36:223–32.
[10] Schmidt Robert, Case Eldon, Ni Jennifer, Sakamoto Jeffrey, Trejo Rosa, Lara-Curzio Edgar, et al. The temperature dependence of thermal expansion for p-type Ce0. 9Fe3. 5Co0. 5Sb12 and n-type Co0. 95Pd0. 05Te0. 05Sb3 skutterudite thermoelectric materials. Phil Mag 2012;92(10):1261–86.
[11] Witting Iyan, Grovogui Jann, Dravid Vinayak, Snyder Jeffrey, et al. Thermoelectric transport enhancement of Te-rich bismuth antimony telluride (Bi0. 5Sb1. 5Te3+ x) through controlled porosity. J Materiomics 2020;6(3):532–44.
[12] Schmitz Andreas, Stiewi Christian, Zabrocki Knud, De Boor Johannes, Mull Klaus, Müller Eckhard, et al. Current assisted sintering of PbTe—effects on thermoelectric and mechanical properties. Mater Res Bull 2017;86:159–66.
[13] Takashiri M, Tanaka S, Miyazaki K. Determination of the origin of crystal orientation for nanocrystalline bismuth telluride-based thin films prepared by use of the flash evaporation method. J Electron Mater 2014;43(6):1881–9.
[14] Biguereau E, Bouvard D, Chaix JM, Roure S, et al. On the swelling of silver powder during sintering. Powder Metall 2016;59(5):394–400.
[15] Lee Hohyun, Daryoosh Vashaee, D.Z. Wang, Mildred Dresselhaus, Z.F. Ren, Gang Chen, et al. Effects of nanoscale porosity on thermoelectric properties of SiGe. J Appl Phys 2010;107(9):94308.
[16] Wang Shiren, Tambraparni Madhava, Qiu Jingjing, Tipton John, Dean Derrick, et al. Thermal expansion of graphene composites. Macromolecules 2009;42(14):5251–5.
[17] Liang Aoyan, Jiang Xiaosong, Hong Xin, Jiang Yixin, Shao Zhyenyi, Zhu Degui, et al. Recent developments concerning the dispersion methods and mechanisms of graphene. Coatings 2018;8(1):33.
[18] Yu Zhenhe, Yang Wenshu, Zhou Chang, Zhang Ningbo, Chao Zhenlong, Liu Hao, et al. Effect of ball milling time on graphene nanosheets reinforced Al6063 composite fabricated by pressure infiltration method. Carbon 2019;141:25–39.
[19] Tang Huaichao, Sun Fu-Hua, Dong Jin-Feng, Asfandiyar, Zhuang Hua-Lu, Pan Yu, et al. Graphene network in copper sulfide leading to enhanced thermoelectric properties and thermal stability. Nano Energy 2018;49:267–73.
[20] Zhao Li-Dong, Lo Shih-Han, Zhang Yongsheng, Sun Hui, Tan Gangjian, Uher Ctirad, et al. Ultralow thermal conductivity and high thermoelectric figure of merit in SnSe crystals. Nature 2014;508(7496):373–7.
[21] Wang Wen-ting, Zheng Zhuang-hao, Li Fu, Li Cao, Fan Ping, Luo Jing-Ting, et al. Synthesis process and thermoelectric properties of n-type tin selenide thin films. J Alloys Compd 2018;763:960–5.
[22] Hernandez Jose, Ruiz Angel, Fonseca Luis, Pettes Michael, Jose-Yacaman Miguel, Benitez Alfredo, et al. Thermoelectric properties of SnSe nanowires with different diameters. Sci Rep 2018;8(1):1–8.
[23] Burton Matthew, Liu Tianjun, McGettrick James, Mehraban Shahin, Baker Jenny, Pockett Adam, et al. Thin film tin selenide (SnSe) thermoelectric generators exhibiting ultralow thermal conductivity. Adv Mater 2018:1801357.
[24] Chen Cheng-Lung, Wang Heng, Chen Yang-Yuan, Day Tristan, Snyder G Jeffrey, et al. Thermoelectric properties of p-type polycrystalline SnSe doped with Ag. J Mater Chem 2014;2(29):11171–6.
[25] Fu Yajie, Xu Jingtao, Liu Guo-Qiang, Tan Xiaojian, Liu Zhu, Wang Xue, et al. Study on thermoelectric properties of polycrystalline SnSe by Ge doping. J Electron Mater 2017;46(5):3182–6.
[26] Li JC, Li D, Qin XY, Zhang J, et al. Enhanced thermoelectric performance of p-type SnSe doped with Zn. Scripta Mater 2017;126:6–10.
[27] Zhang Qian, Chere Eyob, Sun Jingying, Cao Feng, Dahal Keshab, Chen Shuo, et al. Studies on thermoelectric

properties of n-type polycrystalline SnSe1-xSx by iodine doping. Adv Energy Mater 2015;5(12):1500360.
[28] Leng Hua- Qian, Zhou Min, Han Ye-Mao, Li Lai-Feng, et al. The thermoelectric performance of anisotropic SnSe doped with Na. RSC Adv 2016;6(11):9112–6.
[29] Chere Eyob, Zhang Qian, Dahal Keshab, Cao Feng, mao Jun, Ren Zhifeng, et al. Studies on thermoelectric figure of merit of Na-doped p-type polycrystalline SnSe. J Mater Chem 2016;4(5):1848–54.
[30] Li Shan, Wang Yumei, Chen Chen, Li Xiaofang, Xue Wenhua, Wang Xinyu, et al. Heavy doping by bromine to improve the thermoelectric properties of n-type polycrystalline SnSe. Adv Sci 2018;5(9):1800598.
[31] Zhao Qian, Qin Bingchao, Wang Dongyang, Qiu Yuting, Zhao Li-Dong, et al. Realizing high thermoelectric performance in polycrystalline SnSe via silver doping and germanium alloying. ACS Appl Energy Mater 2019;3(3):2049–54.
[32] Li JC, Li D, Xu W, Qin XY, Li YY, Zhang J, et al. Enhanced thermoelectric performance of SnSe based composites with carbon black nanoinclusions. Appl Phys Lett 2016;109(17):173902.
[33] Li D, Li JC, Qin XY, Zhang J, Xin HX, Song CJ, et al. Enhanced thermoelectric performance in SnSe based composites with PbTe nanoinclusions. Energy 2016;116:861–6.
[34] Ju H, Kim J. Effect of SiC ceramics on thermoelectric properties of SiC/SnSe composites for solid-state thermoelectric applications. Ceram Int 2016;42(8):9550–6.
[35] Cai Bowen, Li Jianghua, Sun Hao, Zhao Peng, Yu Fengrong, Zhang Long, et al. Sodium doped polycrystalline SnSe: high pressure synthesis and thermoelectric properties. J Alloys Compd 2017;727:1014–9.
[36] Chien Chia-Hua, Chang Chung-Chieh, Chen Cheng-Lung, Tseng Chuan-Ming, Wu Yu-Ruei, Wu Maw-Kuen, et al. Facile chemical synthesis and enhanced thermoelectric properties of Ag doped SnSe nanocrystals. RSC Adv 2017;7(54):34300–6.
[37] Wubieneh Tessera, Chen Cheng-Lung, Wei Pai Chun, Chen Szu-Yuan, Chen Yang-Yuan, et al. The effects of Ge doping on the thermoelectric performance of p-type polycrystalline SnSe. RSC Adv 2016;6(115):114825–9.
[38] El-Asfoury Mohamed, Nasr Mohamed, Nakamura Koichi, Abdel-Moneim Ahmed, et al. Thermoelectric power factor performance of Bi85Sb15/graphene composite. Jpn J Appl Phys 2016;55(4):45802.
[39] Suh Daewoo, Lee Sanghoon, Mun Hyeona, Park Sung-Hoon, Lee Kyu Hyoung, Kim SungWng, et al. Enhanced thermoelectric performance of Bi0. 5Sb1. 5Te3-expanded graphene composites by simultaneous modulation of electronic and thermal carrier transport. Nano Energy 2015;13:67–76.
[40] Song Jiangxuan, Yu Zhaoxin, Gordin Mikhail, Wang Donghai, et al. Chemically bonded phosphorus/graphene hybrid as a high performance anode for sodium-ion batteries. Nano Lett 2014;14(11):6329–35.
[41] Youssef KM, Scattergood RO, Murty KL, Koch CC, et al. Nanocrystalline Al–Mg alloy with ultrahigh strength and good ductility. Scripta Mater 2006;54(2):251–6.
[42] Zhao Degang, Tian Changwen, Liu Yunteng, Zhan Chengwei, Chen Lidong, et al. High temperature sublimation behavior of antimony in CoSb3 thermoelectric material during thermal duration test. J Alloys Compd 2011;509(6):3166–71.
[43] Li Yi, Heremans Joseph, Zhao Ji-Cheng, et al. High-temperature oxidation behavior of thermoelectric SnSe. J Alloys Compd 2016;669:224–31.
[44] Najimi A, Shahverdi H. Effect of milling methods on microstructures and mechanical properties of Al6061-CNT composite fabricated by spark plasma sintering. Mater Sci Eng, A 2017;702:87–95.
[45] Hiramatsu M, Kondo H, Hori M. Graphene nanowalls. New Progress on Graphene Research; 2013. p. 235–60.
[46] Gao Guodong, Liu Dandan, Tang Shangcheng, Huang Can, He Mengci, Guo Yu, et al. Heat-initiated chemical functionalization of graphene. Sci Rep 2016;6:20034.
[47] Li Min, Gao Haiyan, Liang Jiamiao, Gu Sunwang, You Weren, Shu Da, et al. Microstructure evolution and properties of graphene nanoplatelets reinforced aluminum matrix composites. Mater Char 2018;140:172–8.
[48] Bastwros Mina, Kim Gap-Yong, Zhu Can, Zhang Kun, Wang Shiren, Tang Xiaoduan, et al. Effect of ball milling on graphene reinforced Al6061 composite fabricated by semi-solid sintering. Compos B Eng 2014;60:111–8.
[49] Lee Taegeon, Mas'ud Felisita, Kim Myung, Rho Heesuk, et al. Spatially resolved Raman spectroscopy of defects, strains, and strain fluctuations in domain structures of monolayer graphene. Sci Rep 2017;7(1):1–8.
[50] Alsalama M, Hamoudi H, Youssef KM. The effect of graphene structural integrity on the power factor of tin selenide nanocomposite. J Alloys Compd 2021:159584.
[51] Cui Ye, Wang Lidong, Li Bin, Cao Guojian, Fei Weidong, et al. Effect of ball milling on the defeat of few-layer graphene and properties of copper matrix composites. Acta Metall Sin 2014;27(5):937–43.
[52] Ahn Kyunghan, Cho Eunseog, Rhyee Jong-Soo, Kim Sang, Lee Sang, Lee Kyu, et al. Effect of cationic substitution on the thermoelectric properties of In4-xMxSe2.95 compounds (M = Na, Ca, Zn, Ga, Sn, Pb; x=0.1). Appl Phys Lett 2011;99(10).
[53] Yehia HM, Nouh F, El-Kady O. Effect of graphene nano-sheets content and sintering time on the microstructure, coefficient of thermal expansion, and mechanical properties of (Cu/WC–TiC-Co) nano-composites. J Alloys Compd 2018;764:36–43.
[54] Habiba Khaled, Makarov Vladimir, Avalos Javier, Guinel Maxime, Weiner Brad, Morell Gerardo, et al. Luminescent graphene quantum dots fabricated by pulsed laser synthesis. Carbon 2013;64:341–50.
[55] Lin L, Westwood A, Drummond-Brydson R. Graphene synthesis via electrochemical exfoliation of graphite nanoplatelets in aqueous sulphuric acid. 2016.
[56] Huang Pinshane, Ruiz-Vargas Carlos, van der Zande Arend, Whitney William, Levendrof Mark, Kevek Joshua, et al. Grains and grain boundaries in single-layer graphene atomic patchwork quilts. Nature 2011;469(7330):389–92.
[57] Munir KS, Wen C. Deterioration of the strong sp2 carbon network in carbon nanotubes during the mechanical dispersion processing—a review. Crit Rev Solid State Mater Sci 2016;41(5):347–66.
[58] Yadhukulakrishnan Govindaraajan, Rahman Arif, Karumuri Sriharsha, Stackpoole Margaret, Kalkan A Kaan, Singh Raman, et al. Spark plasma sintering of silicon carbide and multi-walled carbon nanotube reinforced zirconium diboride ceramic composite. Mater Sci Eng, A 2012;552:125–33.
[59] Sun Jialin, Zhao Jun, Huang Zhifu, Yan Ke, Chen Fei, Jian Yongxin, et al. Preparation and properties of multilayer graphene reinforced binderless TiC nanocomposite cemented carbide through two-step sintering. Mater Des 2020;188:108495.
[60] Yadhukulakrishnan Govindaraajan, Karumuri Sriharsha, Rahman Arif, Singh Raman, Kalkan AKan, Harimkar Sandip, et al. Spark plasma sintering of graphene reinforced zirconium diboride ultra-high temperature ceramic composites. Ceram Int 2013;39(6):6637–46.
[62] Shi Xiaolei, Wu Angyin, Liu Weidi, Moshwan Raza, Wang Yuan, Chen Zhi-Gang, et al. Polycrystalline SnSe with extraordinary thermoelectric property via nanoporous design. ACS Nano 2018;12(11):11417–25.